

Helical spin thermoelectrics controlled by a side-coupled magnetic quantum dot in the quantum spin Hall state

Pablo Roura-Bas,¹ Liliana Arrachea,^{2,3} and Eduardo Fradkin⁴

¹*Centro Atómico Bariloche, CNEA, 8400 S. C. de Bariloche, Argentina*

²*International Center for Advanced Studies, Escuela de Ciencia y Tecnología, Universidad Nacional de San Martín, 25 de Mayo y Francia, 1650 Buenos Aires, Argentina*

³*Kavli Institute for Theoretical Physics, Kohn Hall, University of California at Santa Barbara, Santa Barbara, California 93106, USA*

⁴*Department of Physics and Institute for Condensed Matter Theory, University of Illinois at Urbana-Champaign, 1110 West Green Street, Urbana, Illinois 61801-3080, USA*



(Received 25 August 2018; published 19 November 2018)

We study the thermoelectric response of a device containing a pair of helical edge states contacted at the same temperature T and chemical potential μ and connected to an external reservoir, with different chemical potential and temperature, through a side quantum dot. Different operational modes can be induced by applying a magnetic field B and a gate voltage V_g at the quantum dot. At finite B , the quantum dot acts simultaneously as a charge and a spin filter. Charge and spin currents are induced, not only through the quantum dot, but also along the edge states. We focus on linear response and analyze the regimes, which we identify as charge heat engines or refrigerator, spin heat engine, and spin refrigerator.

DOI: [10.1103/PhysRevB.98.195429](https://doi.org/10.1103/PhysRevB.98.195429)

I. INTRODUCTION

One of most remarkable properties of topological insulating phases is the existence of conducting edge states. In two-dimensional systems, such as in the quantum Hall state or the spin quantum Hall (QSH) state, these edge states are single or multiple one-dimensional (1D) channels through which charge and energy propagate only in one direction. In the case of the quantum Hall, the edge states are chiral [1–5] as a consequence of the broken time-reversal symmetry. Instead, the QSH hosts Kramers pairs of helical counterpropagating edge states with opposite spin orientation [6–11]. In situations where the electron-electron interactions play a role, these systems exhibit another extraordinary feature: the fractionalization of the charge and spin in the low-energy excitations. This has an impact in the unidirectional transport properties along the edges [1,5,12,13], as well as through tunneling contacts to other edge states or to other structures like quantum dots [14–20]. The edge states of the fractional quantum Hall effect are well described as chiral Luttinger liquids and the fractional charge is directly related to the magnetic filling factor [1,5]. A pair of edge states of the QSH is effectively described by a Luttinger liquid of left and right moving electrons where spin and charge fractionalization can take place as a consequence of the Coulomb interaction represented by a parameter K [5,21].

Thermal transport in edge states of the quantum Hall regime has received a great deal of attention for some time. Since the pioneer works by Kane and Fisher [12,13], several studies were reported on heat transport in the integer [22–25] and in the fractional regimes [26–35]. More recently, thermoelectric effects have also been explored in the integer [36,37], as well as in the fractional case [20,38]. Relatively less is presently known about thermal transport and thermoelectric effects in the quantum spin Hall regime [39–45].

Tunneling contacts to quantum dots in mesoscopic structures play a crucial role in the thermoelectric response of these systems. This is because they enable transport with broken particle-hole symmetry, which is a necessary condition for realizing the charge to energy conversion characteristic of thermoelectricity [46–50]. Charge transport in helical edges of the quantum spin Hall regime with tunneling contacts between edge states and quantum dots or antidots is a subject of very active theoretical investigation [51–67].

The aim of the present work is to analyze the thermoelectric response of quantum spin Hall helical edges realized in the structure sketched in Fig. 1. It consists of a pair of helical edge states of a quantum spin Hall system

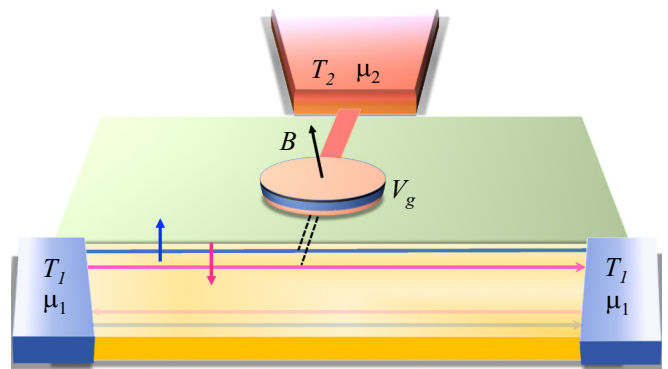


FIG. 1. Sketch of the setup. A Kramers pair of helical edge states of the spin Hall effect is ballistically contacted to terminals at temperature T_1 and chemical potential μ_1 , while tunneled contacted to an external reservoir at a different temperature T_2 and chemical potential μ_2 through a quantum dot. The transport through the quantum dot can be controlled by means of a gate voltage and a weak magnetic field B .

connected to an external reservoir at a different temperature and chemical potential, through a tunneled-coupled quantum dot. The transport through the quantum dot is controlled by means of a gate voltage and a magnetic field. As we will discuss, the physics of this device is very rich, allowing for the implementation of a variety of thermoelectric regimes, taking advantage of the helical nature of the edge states. The possibility of the magnetic control of the charge flow in helical edges was explored in other setups with magnetic islands in direct contact to the edge states [68–70]. Here we consider the effect of a Zeeman field on the side-coupled dot of the structure of the figure, in order to introduce spin filtering of the electrons injected from the external reservoir. The magnetic field is localized at the quantum dot and it is weak enough to leave the helical edge states unaffected. With these ingredients we have not only heat-charge conversion, but also heat-spin conversion.

Without the ingredient of the magnetic field at the quantum dot, the setup of the figure may operate as a charge heat engine, or refrigerator, as is usual in thermoelectric devices where heat flows induced by temperature differences can be used to generate charge currents against chemical potential differences and vice versa. The magnetic field at the quantum dot adds the possibility of inducing spin currents, not only through the quantum dot, but also through the helical channels between the left and right terminals of the QSH bar. This comes along with heat flow between these two terminals, even when they are assumed to be at the same temperature and chemical potential. We identify two relevant operational regimes introduced by the spin filtering, which we name the spin heat engine and the spin refrigerator, respectively. We analyze in detail all these regimes. On the other hand, the fractionalization of charge and energy in chiral Luttinger liquids has the consequence of enhancing the thermoelectric performance of the fractional quantum Hall regime, relative to the integer case, described by noninteracting electrons [20]. We show that the Coulomb repulsion represented by the Luttinger parameter K has a similar effect in the present case.

The paper is organized as follows. In Sec. II we present the theoretical model for the setup of Fig. 1. In Sec. III we present the theoretical framework to analyze its thermoelectric response. We present results for the different operational modes in Sec. IV. Summary and conclusions are presented in Sec. V.

II. MODEL

The theoretical model for the setup of Fig. 1 is defined by the following Hamiltonian:

$$H = H_{\text{edges}} + H_{\text{dot}} + H_{\text{tun}}, \quad (1)$$

where the first term correspond to the pair of helical edges. It is modeled as a Luttinger liquid as follows [5,21]:

$$H_{\text{edges}} = \frac{v}{4\pi K} \int dx \{ [\partial_x \phi_{\uparrow}(x)]^2 + [\partial_x \phi_{\downarrow}(x)]^2 \}. \quad (2)$$

Notice that due to the helical nature of the edge states, the direction of propagation is determined by the spin orientation. Hence, the spin labels \uparrow and \downarrow denote at the same time left

and right moving excitations propagating with velocity v . The Coulomb electron-electron interaction is characterized by the parameter K , such that $K < 1$ ($K > 1$) corresponds to repulsive (attractive) interactions and $K = 1$ corresponds to the noninteracting case. The densities $\partial_x \phi_{\sigma}(x)$ are expressed in terms of bosonic modes obeying a Kac Moody algebra

$$[\phi_{\downarrow}(x), \phi_{\downarrow}(x')] = -[\phi_{\uparrow}(x), \phi_{\uparrow}(x')] = i\pi K \text{sgn}(x - x'). \quad (3)$$

They are related to fermionic fields through

$$\psi_{\downarrow, \uparrow}(x) = \frac{F_{\downarrow, \uparrow}}{\sqrt{2\pi a}} e^{i[K_{\pm} \phi_{\downarrow}(x) + K_{\mp} \phi_{\uparrow}(x)]}, \quad (4)$$

with a being a characteristic length and

$$K_{\pm} = (K^{-1} \pm 1)/2. \quad (5)$$

The Klein factors F_{σ} ensure $\{\psi_{\sigma}(x), \psi_{\sigma'}(x')\} = \delta_{\sigma, \sigma'} \delta(x - x')$.

The second term of Eq. (1) describes a quantum dot side coupled to the QSH bar. It is controlled by a gate voltage V_g and a magnetic field B , which has components B_{\parallel} , parallel, and B_{\perp} , perpendicular, to the direction of the spin-orbit coupling of the QSH system. We focus on the situation where the magnetic field is strongly localized at the side-coupled quantum dot and weak enough to preserve the time-reversal invariance of the QSH bar. For simplicity we consider a single-level quantum dot,

$$H_{\text{dot}} = \sum_{\sigma} \varepsilon_{d\sigma} d_{\sigma}^{\dagger} d_{\sigma} + \varepsilon_{\perp} (d_{\uparrow}^{\dagger} d_{\downarrow} + \text{H. c.}), \quad (6)$$

with $\varepsilon_{d, \sigma} = eV_g + s_{\sigma} \mu_B B_{\parallel}/2$, $s_{\uparrow, \downarrow} = \pm$, and $\varepsilon_{\perp} = \mu_B B_{\perp}/2$. It is convenient to diagonalize the Hamiltonian for the dot as follows:

$$H_{\text{dot}} = \sum_{s=\pm} E_s d_s^{\dagger} d_s. \quad (7)$$

The local energies in the diagonal basis read

$$E_s = eV_g \pm \mu_B \frac{B}{2}, \quad B = \sqrt{B_{\parallel}^2 + B_{\perp}^2}. \quad (8)$$

The change of basis is $d_s = \sum_{\sigma} u_{s, \sigma} d_{\sigma}$, with

$$\begin{aligned} u_{+, \uparrow} &= \cos(\theta/2), & u_{-, \uparrow} &= \sqrt{1 - u_{+, \uparrow}^2}, \\ u_{+, \downarrow} &= -u_{-, \uparrow}, & u_{-, \downarrow} &= u_{+, \uparrow}, \end{aligned} \quad (9)$$

where the angle θ is determined by $\cos(\theta) = B_{\parallel}/B$.

The quantum dot is tunneled coupled to the helical edges with amplitudes w_{σ} [18] and also to an external reservoir of ordinary fermions with amplitude w . The Hamiltonian reads

$$H_{\text{tun}} = \sum_{\sigma} w_{\sigma} d_{\sigma}^{\dagger} \psi_{\sigma}(x=0) + w \sum_{\sigma, k} d_{\sigma}^{\dagger} c_{k\sigma} + \text{H. c.} \quad (10)$$

III. LINEAR THERMOELECTRIC DESCRIPTION

A. Spin-dependent fluxes and Onsager matrix

We assume that the quantum dot is strongly coupled to the external reservoir, so that it has the same chemical potential $\mu_2 = \mu$ and temperature $T_2 = T + \Delta T$ of this system. The edge states are contacted to left and right reservoirs at chemical potential $\mu_1 = \mu + eV$ and $T_1 = T$. The charge and heat

currents between the quantum dot and the helical edges is composed of fluxes of \uparrow electrons flowing to the L channel and \downarrow electrons flowing to the R channel. We set $\mu = 0$, and define these components as follows:

$$\begin{aligned} J_{\sigma}^C &= -2e w_{\sigma} \text{Re}[G_{d,\sigma}^<(t, t)], \\ J_{\sigma}^Q &= -2w_{\sigma} \text{Re}[i \partial_{t'} G_{d,\sigma}^<(t, t')]_{t'=t}, \end{aligned} \quad (11)$$

where we have introduced the lesser Green's function $G_{d,\sigma}^<(t, t') = -i \langle d_{\sigma}^{\dagger}(t) \psi_{\sigma}(t') \rangle$. In the next section we will explain the method to evaluate these currents. Here we focus on small temperature differences ΔT and small bias voltages eV between the reservoirs contacting the edges and the reservoir contacting the quantum dot. Under this condition, these currents will be linear functions of the affinities $X_1 = \Delta\mu/T$ and $X_2 = \Delta T/k_B T^2$, with $\Delta\mu = \mu_2 - \mu_1$ and $\Delta T = T_2 - T_1$,

$$\begin{aligned} J_{\sigma}^C &= L_{11}^{\sigma} X_1 + L_{12}^{\sigma} X_2, \\ J_{\sigma}^Q &= L_{21}^{\sigma} X_1 + L_{22}^{\sigma} X_2. \end{aligned} \quad (12)$$

The coefficients L_{ij}^{σ} obey Onsager relations $L_{ij}^{\uparrow}(B) = L_{ji}^{\downarrow}(-B)$. In addition, these coefficients satisfy constraints imposed by the second law of thermodynamics, according to which the rate of entropy production is positive [47,48],

$$\dot{S} = \sum_{i,j} X_i L_{ij} X_j \geq 0, \quad (13)$$

with $L_{ij} = \sum_{\sigma} L_{ij}^{\sigma}$. This implies $L_{11}, L_{22} \geq 0$, $\det[L] \geq 0$.

The diagonal matrix elements define, respectively, the electrical and thermal conductances per spin channel, while the off-diagonal matrix elements define the charge to energy conversion and vice versa. For $B \neq 0$, the charge current comes along with a spin current. In turn, imbalance between the flows with \uparrow and \downarrow electrons implies a net spin current flowing into the left or right terminal of the QSH bar. Therefore, we can identify different thermoelectric operational modes for this setup, which we describe below.

B. Operational modes

The different interesting operational modes are: charge heat engine or refrigerator, spin heat engine, and spin refrigerator. They are illustrated in Figs. 2 and 3. While the charge heat engine or refrigerator mode can be realized with magnetic field as well as without magnetic field, the spin heat engine and spin refrigerator modes operate only with a finite magnetic field. The conditions of operation corresponding to each case are indicated in Sec. V.

1. Charge heat engine or refrigerator

We start by considering the cases sketched in Fig. 2. These are the usual operational modes of a two-terminal configuration with chemical potential and a temperature differences in opposition. In our case, the hot terminal is the quantum dot connected to the reservoir at μ and $T + \Delta T$, while the cold reservoir is the Luttinger liquid composed of the two helical edge states. The thermoelectric response can be described by

$$\begin{pmatrix} J^C \\ J^Q \end{pmatrix} = \begin{pmatrix} \mathcal{L}_{11}^c & \mathcal{L}_{12}^c \\ \mathcal{L}_{21}^c & \mathcal{L}_{22}^c \end{pmatrix} \begin{pmatrix} X_1 \\ X_2 \end{pmatrix}. \quad (14)$$

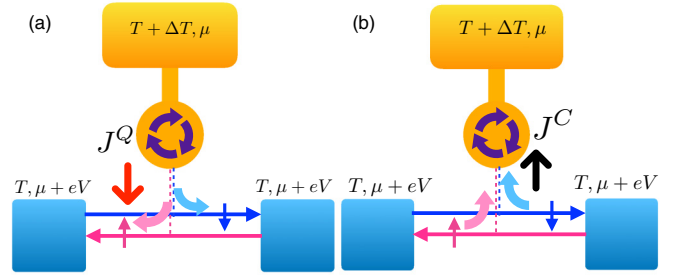


FIG. 2. (a) Charge heat engine. The heat current from the hottest reservoir is converted into charge current flowing through the tunneling contact and equally distributed, in absence of magnetic field, to the left and right reservoir of the QSH system. (b) Charge refrigerator. An electric current flows from the edge states to the quantum dot and is accompanied by a heat current that refrigerates the left and right reservoirs of the QSH system.

In terms of the fluxes and Onsager coefficients defined in Eq. (12) we have $J^C = \sum_{\sigma} J_{\sigma}^C$, $J^Q = \sum_{\sigma} J_{\sigma}^Q$, and $\mathcal{L}_{ij}^c = \sum_{\sigma} L_{ij}^{\sigma}$. The device can operate as a heat engine or refrigerator. The performance of these operational modes is qualified by the efficiency (heat engine) or coefficient of performance (refrigerator) as follows:

$$\eta^{c,\text{he}} = -\frac{J^C X_1}{J^Q}, \quad \eta^{c,\text{fri}} = -\frac{J^Q}{J^C X_1}. \quad (15)$$

In the former case J^C flows against the bias voltage X_1 and an electrical power $-J^C X_1$ is generated at expenses of the investment of a heat flow J^Q , while in the latter case a heat current $-J^Q$ is extracted from the coldest reservoir by investing an electrical power $J^C X_1$. Both coefficients are bounded by the Carnot limits $\eta^{c,\text{he}} \leq \Delta T/T$ and $\eta^{c,\text{fri}} \leq T/\Delta T$.

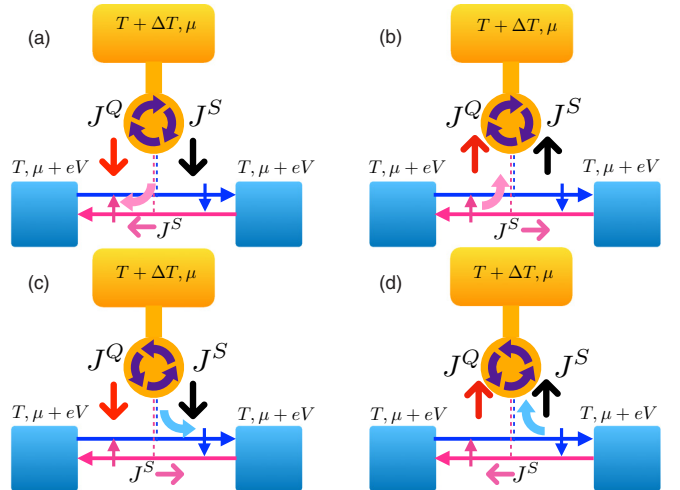


FIG. 3. (a) and (c) Spin heat engine. The heat current from the hottest reservoir is converted into a spin current flowing through the tunneling contact and to the left (for \uparrow electrons) and right (for \downarrow electrons) reservoir of the QSH system. (b) and (d) Spin refrigerator. A polarized (\uparrow or \downarrow) electric current flows from the edge states to the quantum dot and is accompanied by a refrigeration of the left or right reservoirs of the QSH system.

2. Spin heat engine

We now consider the cases sketched in Figs. 3(a) and 3(c). The magnetic field at the quantum dot filters electrons with a given spin component. The heat current flowing from the hot reservoir in strong coupling to the quantum dot leads to a polarized electron current through the tunneling contact to the helical edge states and a spin current is induced at the QSH system. Due to the helical nature of the edge states, this also implies a charge current flowing to the left or to the right along the edge. Hence the direction of the magnetic field distributes the electron flow towards the left or right terminals of the QSH bar. The thermoelectric description to characterize the generation of a spin current J^S in the QSH by using the heat current J^Q can be formulated in terms of the linear dependence of these currents with the affinities,

$$\begin{pmatrix} J^S \\ J^Q \end{pmatrix} = \begin{pmatrix} \mathcal{L}_{11}^s & \mathcal{L}_{12}^s \\ \mathcal{L}_{21}^c & \mathcal{L}_{22}^c \end{pmatrix} \begin{pmatrix} X_1 \\ X_2 \end{pmatrix}, \quad (16)$$

with $J^S = \xi(J_\uparrow^C - J_\downarrow^C)$, where $\xi = \text{sgn}(L_{11}^\uparrow - L_{11}^\downarrow)$. The matrix elements of Eq. (16) in terms of the original Onsager coefficients read $\mathcal{L}_{1j}^s = \xi(L_{1j}^\uparrow - L_{1j}^\downarrow)$ and \mathcal{L}_{2j}^c . We have introduced the sign ξ in the definition, in order to have $\mathcal{L}_{11}^s > 0$ and J^Q is the total heat current previously defined. In this case, the efficiency is quantified as the ratio between fraction of the electrical power flowing against the bias voltage to the left or right terminals (for $\xi > 0$ or $\xi < 0$), $-J^S X_1$, and the heat current flowing from the hot reservoir J^Q ,

$$\eta^{s,\text{he}} = -\frac{J^S X_1}{J^Q}. \quad (17)$$

Notice that $J^S X_1$ has the same units as the electrical power, since J^S is a polarized charge current.

3. Spin refrigerator

Finally we consider the cases sketched Figs. 3(b) and 3(d). They can be regarded as the reversed operational mode of the spin heat engine. As a consequence of the spin filtering introduced by the magnetic field, not only a polarized electron flux but also an associated energy flux is established between the left and right terminals of the QSH bar. This can be described by the heat current $J^{Q,s} = \xi(J_\uparrow^Q - J_\downarrow^Q)$, with $\xi = \text{sgn}(L_{22}^\uparrow - L_{22}^\downarrow)$. Hence, a polarized charge flux from the helical edges towards the quantum dot and the external terminal can be used to refrigerate the left or the right reservoir contacting the QSH system. The thermoelectric response can be described as follows:

$$\begin{pmatrix} J^C \\ J^{Q,s} \end{pmatrix} = \begin{pmatrix} \mathcal{L}_{11}^c & \mathcal{L}_{12}^c \\ \mathcal{L}_{21}^s & \mathcal{L}_{22}^s \end{pmatrix} \begin{pmatrix} X_1 \\ X_2 \end{pmatrix}, \quad (18)$$

The matrix elements of Eq. (18) in terms of the original Onsager coefficients read $\mathcal{L}_{2j}^s = \xi(L_{2j}^\uparrow - L_{2j}^\downarrow)$ and the efficiency can be quantified as the heat current extracted from the left or the right reservoirs (for $\xi > 0$ or $\xi < 0$), upon investing a total electrical power $J^C X_1$,

$$\eta^{s,\text{fri}} = -\frac{J^{Q,s}}{J^C X_1}. \quad (19)$$

IV. CALCULATION OF THE ONSAGER COEFFICIENTS

The spin-dependent charge and heat currents defined in Eqs. (11) can be calculated by means of nonequilibrium Schwinger Keldysh formalism and treating perturbatively the tunneling couplings between the quantum dot and the helical edges w_σ . Here we summarize the main steps of this calculation. The charge current can be expressed as follows:

$$J_\sigma^C = -2e w_\sigma^2 \int_{-\infty}^{+\infty} dt \sum_{s=\pm} \text{Re} [g_{d,s}^<(t) u_{s,\sigma}^2 g_\sigma^>(-t) - g_{d,s}^>(t) u_{s,\sigma}^2 g_\sigma^<(-t)], \quad (20)$$

where $u_{s,\sigma}$ are defined in Eq. (9). The lesser and greater Green's functions of the quantum dot contacted only to the ordinary reservoir read $g_{ds}^{\lambda^>,<}(t) = \int d\omega e^{-i\omega/\hbar t} \lambda^{\lambda^>,<}(\omega) \rho_{ds}(\omega)$. They depend on the density of states of the quantum dot coupled to the external reservoir,

$$\rho_{ds}(\omega) = \frac{1}{\pi} \frac{\gamma}{\omega - E_s + i\gamma}. \quad (21)$$

The functions $\lambda^<(\omega) = i f_d(\omega)$ and $\lambda^>(\omega) = -i[1 - f_d(\omega)]$ depend on the chemical potential μ and temperature $T + \Delta T$ of the external reservoir in strong coupling with the quantum dot through the Fermi function $f_d(\omega)$. The functions $g_\sigma^{\lambda^>,<}(t)$ correspond to the left moving (for $\sigma = \uparrow$) and right moving (for $\sigma = \downarrow$) electrons at the edge states. They can be written as $g_\sigma^>(t) = -g_\sigma^<(-t)$, with

$$g_\sigma^<(t) = \frac{i}{\hbar} \int d\omega e^{-i\omega/\hbar t} \rho_\sigma(\omega) f_\sigma(\omega + eV), \quad (22)$$

$$\rho_\sigma(\omega) = a^{\bar{K}-1} \frac{(2\pi T)^{\bar{K}-1}}{\Gamma(\bar{K})} \left| \frac{\Gamma(\bar{K}/2 + i\omega/2\pi T)}{\Gamma(1/2 + i\omega/2\pi T)} \right|^2. \quad (23)$$

$\rho_\sigma(\omega)$ is the density of states of the chiral Luttinger liquid of left (for \uparrow) and right (for \downarrow) movers, $\Gamma(x)$ is the Gamma function, and

$$\bar{K} = (K + 1/K)/2. \quad (24)$$

More details on this calculation are presented in the Appendix A.

Substituting these equations in Eq. (20) we get the following expression for the charge current through the tunneling contact:

$$J_\sigma^C = \frac{e}{\hbar} \int_{-\infty}^{+\infty} d\omega \mathcal{T}_\sigma(\omega) [f_\sigma(\omega + eV) - f_d(\omega)],$$

with

$$\mathcal{T}_\sigma(\omega) = 4\pi w_\sigma^2 \sum_s u_{s,\sigma}^2 \rho_{d,s}(\omega) \rho_\sigma(\omega + eV). \quad (25)$$

Similarly, for the heat current we get

$$J_\sigma^Q = \int_{-\infty}^{+\infty} d\omega \frac{\omega}{\hbar} \mathcal{T}_\sigma(\omega) [f_\sigma(\omega + eV) - f_d(\omega)]. \quad (26)$$

Expanding these expressions up to linear order in eV and ΔT we get the Onsager coefficients of Eq. (12),

$$\hat{L}^\sigma = -\frac{k_B T}{2\hbar} \int d\omega \begin{pmatrix} e & e\omega \\ \omega & \omega^2 \end{pmatrix} \mathcal{T}_\sigma(\omega) \frac{\partial f(\omega)}{\partial \omega}. \quad (27)$$

In the limit of low temperature $k_B T < \gamma$, the density of states of the Luttinger liquid can be well approximated by a power law as in Ref. [20]. The resulting expressions for the Onsager coefficients in this limit are

$$\begin{aligned} L_{11}^\sigma &\simeq T \sum_s u_{s,\sigma}^2 \rho_{d,s}(0) I_0(\bar{K}), \\ L_{12}^\sigma &\simeq T \sum_s u_{s,\sigma}^2 \rho'_{d,s}(0) I_2(\bar{K}), \quad L_{21}^\sigma \simeq L_{12}^\sigma, \\ L_{22}^\sigma &\simeq T \sum_s u_{s,\sigma}^2 \rho_{d,s}(0) I_2(\bar{K}), \end{aligned} \quad (28)$$

with

$$I_n(\bar{K}) = c(\bar{K}, T) \frac{(k_B T)^{\bar{K}-1+n}}{\bar{K}-1+n}, \quad (29)$$

where $c(\bar{K}, T)$ is a coefficient depending on \bar{K} and T . Interestingly, from the definition of Eq. (24) we see that \bar{K} is a function of the Luttinger parameter K obeying the following symmetry $K \leftrightarrow 1/K$. Hence, \bar{K} has the same behavior for repulsive ($K < 1$) and attractive ($K > 1$) interactions. This is because the infinite Luttinger liquid for the pair of edge states defined in Eq. (2) can be described in terms of two Hamiltonians, which are bilinear in bosonic fields resulting from combinations of the original ones ϕ_σ . These two Hamiltonians are related by a duality transformation under the change $K \leftrightarrow 1/K$, being the noninteracting case, $K = 1$ self-dual. The local tunneling density of states depends on the two combinations of bosonic fields, hence, on the parameter \bar{K} defined in Eq. (24) [71].

V. RESULTS

A. Charge heat engine and refrigerator

In the operational modes introduced in Sec. III B 1 it is possible to proceed as in the usual 2×2 thermoelectric devices [47] and parametrize the efficiency by a figure of merit

$$ZT = \frac{(\mathcal{L}_{12}^c)^2}{\text{Det} \hat{\mathcal{L}}^c}, \quad (30)$$

with $\mathcal{L}_{12}^c = \mathcal{L}_{21}^c$. $\hat{\mathcal{L}}$ is the Onsager matrix characterizing the corresponding operational mode and \mathcal{L}_{ij}^c the corresponding matrix elements. Following Ref. [47], we can choose $\Delta\mu = -eV$ and $\Delta T > 0$, and derive the maximum efficiency for a fixed ΔT . It can be expressed as

$$\eta^{\max} = \eta_C \frac{\sqrt{ZT + 1} - 1}{\sqrt{ZT + 1} + 1}, \quad (31)$$

with $\eta_C = \Delta T/T$ the Carnot efficiency for the heat engine regime and $\eta_C = T/\Delta T$ the Carnot coefficient of performance for the refrigerator regimes. This maximum corresponds to the following relation between $\Delta\mu$ and ΔT :

$$T \Delta\mu = -\Delta T \frac{\mathcal{L}_{22}^c}{\mathcal{L}_{12}^c} \left(1 - \sqrt{\frac{\text{Det} \hat{\mathcal{L}}^c}{\mathcal{L}_{11}^c \mathcal{L}_{22}^c}} \right). \quad (32)$$

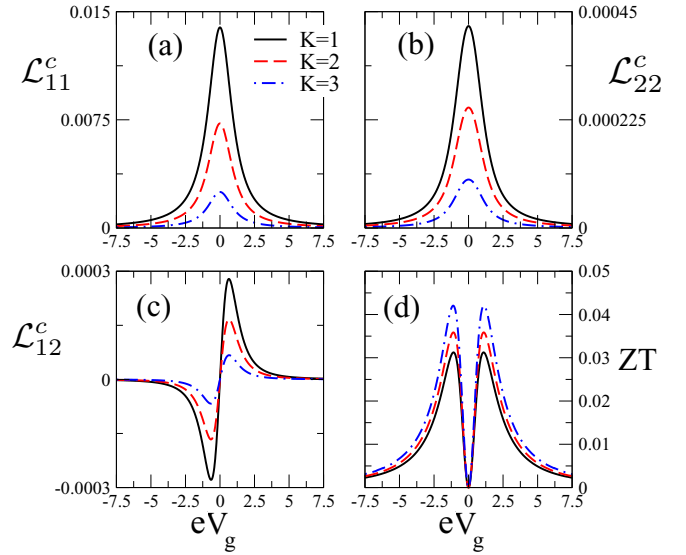


FIG. 4. Onsager coefficients (a), (b), and (c) and figure of merit ZT (d) corresponding at the charge heat engine or refrigerator at the temperature $k_B T = 0.1\gamma$ and $B = 0$, as functions of the gate voltage (in units of γ/e). The unit of \mathcal{L}_{11}^c , \mathcal{L}_{12}^c , \mathcal{L}_{22}^c are, respectively, $e\gamma/h$, $e\gamma^2/h$, γ^3/h . Solid, dashed, and dashed-dotted lines correspond to $K = 1, 2, 3$, respectively.

The device operates as a heat engine within the range of voltages satisfying

$$\begin{aligned} -\frac{\mathcal{L}_{12}^c}{\mathcal{L}_{11}^c} \Delta T \leq T \Delta\mu \leq 0, \quad \mathcal{L}_{12}^c > 0, \\ 0 \leq T \Delta\mu \leq -\frac{\mathcal{L}_{12}^c}{\mathcal{L}_{11}^c} \Delta T, \quad \mathcal{L}_{12}^c < 0, \end{aligned} \quad (33)$$

while it operates as a refrigerator within the range

$$\begin{aligned} T \Delta\mu < -\frac{\mathcal{L}_{22}^c}{\mathcal{L}_{21}^c} \Delta T, \quad \mathcal{L}_{21}^c > 0, \\ T \Delta\mu > -\frac{\mathcal{L}_{22}^c}{\mathcal{L}_{21}^c} \Delta T, \quad \mathcal{L}_{21}^c < 0. \end{aligned} \quad (34)$$

In what follows, we show and analyze the Onsager coefficients and the figure of merit described in the previous section. We calculate numerically the coefficients of Eq. (28) and derive some analytical results based on Eqs. (29) within the low-temperature regime $k_B T < \gamma$. We have verified that the latter are in perfect agreement with the exact results.

1. $B = 0$

In Fig. 4 we show the Onsager coefficients for the charge heat engine or refrigerator described in Sec. III B 1, as well as the corresponding figure of merit. We fix the magnetic field at $B = 0$ a low temperature $T = 0.1\gamma$, and analyze these quantities as functions of the gate voltage.

The diagonal coefficients \mathcal{L}_{11}^c and \mathcal{L}_{22}^c , related, respectively, to the electrical and thermal conductances, have maxima when the level of the dot is aligned with the chemical potential μ . The maximum thermoelectric efficiency, corresponding to the maximum ZT , takes place at the maximum of the absolute value of the off-diagonal coefficient $|\mathcal{L}_{12}^c|$. This is

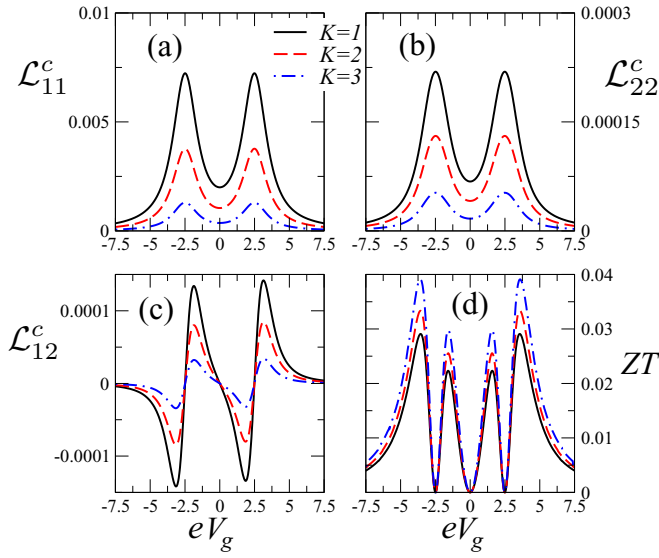


FIG. 5. Onsager coefficients (a), (b) and (c) and figure of merit ZT (d) corresponding at the charge heat engine or refrigerator at the temperature $k_B T = 0.1\gamma$ and magnetic field $B = 5\gamma/\mu_B$ and $\theta = 0$, as functions of the gate voltage. Other details are the same as in Fig. 4.

achieved by applying gate voltages leading to configurations with a high density of states of the quantum dot but with broken particle-hole symmetry. This condition is satisfied within a window $e|V_g| \sim \gamma$. The sign of $\mathcal{L}_{12}^c = \mathcal{L}_{21}^c$ defines the range of voltages for the operational mode, as discussed in Eqs. (34) and (35).

Comparing to the fractional quantum Hall regime, modeled by a chiral Luttinger liquid, we notice that the inverse of the fractional filling factor $1/\nu$ plays a similar role as the parameter \bar{K} defined in Eq. (24) in the present case. Therefore, akin to the fractional quantum Hall effect analyzed in Ref. [20], the thermoelectric performance is enhanced when the system departs from the noninteracting limit $K = 1$. This is true for $K > 1$ as well as $K < 1$.

2. Effect of the magnetic field

Although the magnetic field is not essential for the device to operate as a charge heat engine or refrigerator, it is interesting to analyze its effect. Turning on the magnetic field B , the electronic levels of the quantum dot is split by Zeeman effect into two levels with energies E_{\pm} given in Eq. (8). Figure 5 shows the thermoelectric coefficients and the figure of merit for a finite magnetic field aligned with the direction of the spin-orbit coupling of the QSH bar, $\theta = 0$. We can identify in the behavior of the diagonal coefficients \mathcal{L}_{11}^c and \mathcal{L}_{22}^c as functions of the gate voltage (top panels) the two peaks at $eV_g = \pm\mu_B B/2$. These correspond to the values of the gate voltage for which the levels are aligned with the mean chemical potential μ . Concomitantly, the nondiagonal coefficient \mathcal{L}_{12}^c also presents more features than in the case of vanishing magnetic field. In particular, this coefficient vanishes at the two resonant values $eV_g = \pm\mu_B B/2$, in addition to the particle-hole symmetric value $eV_g = 0$ of the zero magnetic field.

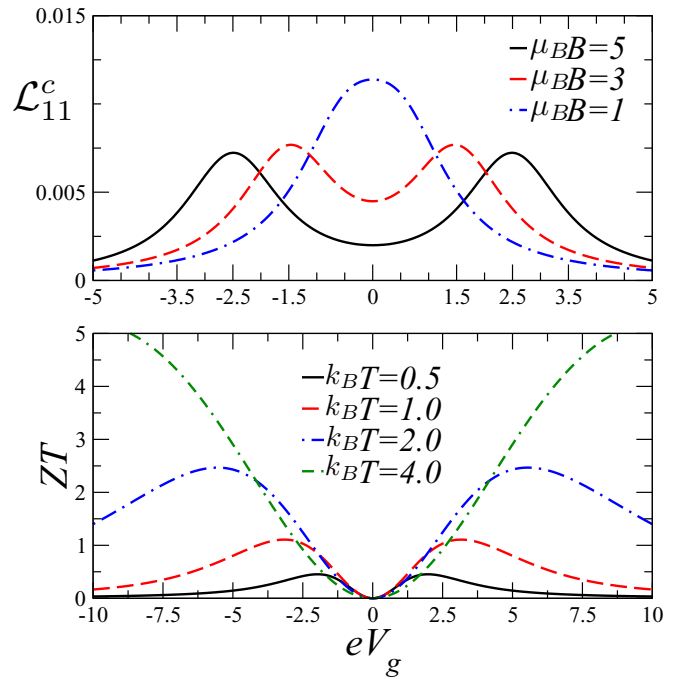


FIG. 6. Top panel: Diagonal coefficient \mathcal{L}_{11}^c at the temperature $k_B T = 0.1\gamma$ and $\theta = 0$ and $K = 1$ for several values of the magnetic field as a function of the gate voltage. Lower panel: Figure of merit at zero magnetic field for several values of temperature and $K = 1$. The operational mode is charge heat engine or refrigerator. Other details are the same as in Fig. 5.

Changing the direction of the applied magnetic field θ has no effect on the Onsager coefficients \mathcal{L}_{ij}^c . This result can be understood on the basis of the expressions given in Eq. (29). Considering, for instance, the case of the low-temperature expression for the coefficient

$$\begin{aligned} \mathcal{L}_{11}^c &= \sum_{\sigma} L_{11}^{\sigma} \simeq T \sum_{s,\sigma} u_{s,\sigma}^2 \rho_{d,s}(0) I_0(\bar{K}) \\ &= T \sum_s \rho_{d,s}(0) I_0(\bar{K}), \end{aligned} \quad (35)$$

and taking into account that from Eq. (9) $\sum_{\sigma} u_{s,\sigma}^2 = 1$, we conclude that the component B_{\perp} of the magnetic field does not play any role in this regime. This is also true for the exact coefficients evaluated numerically. Hence, the perfect alignment of the magnetic field along the direction of the spin-orbit axis of the topological insulator is not crucial for the thermoelectric performance of this operational mode.

In the top panel of Fig. 6 we show the behavior of \mathcal{L}_{11}^c for several values of the magnetic field. When the magnitude of the magnetic field is reduced we observe a decreasing resolution of the peaks located at the energies of the dot in the diagonal coefficients. Both peaks merge into a single peak for values of the applied field approaching the intrinsic broadening γ of the quantum dot levels. The effect of the temperature is analyzed in the lower panel of Fig. 6. As the temperature is increased, large values of the figure of merit are achieved. This is similar to the results for the fractional quantum Hall effect presented in Ref. [20]. Substituting the low-temperature behavior for the Onsager coefficients given

by Eqs. (29) we get the following analytical behavior for the low-temperature regime:

$$ZT \sim \left(\frac{\rho'_d(0)}{\rho_d(0)} \right)^2 \frac{\bar{K}^2 - 1}{(\bar{K} + 1)^2} (k_B T)^2, \quad K \neq 1,$$

$$ZT \sim \left(\frac{\rho'_d(0)}{\rho_d(0)} \right)^2 (k_B T)^2, \quad K = 1. \quad (36)$$

The above expression is in perfect agreement with the analytical results.

B. Spin heat engine

For the spin heat engine mode described in Sec. III B 2, we are interested in the conversion of the heat current from the external reservoir to a spin current through the quantum dot and along the edge states of the QSH bar. This mode can only be implemented by applying a magnetic field at the quantum dot. To characterize it, we introduced the coefficients \mathcal{L}_{11}^s and \mathcal{L}_{12}^s in Eq. (16) to describe the linear dependence of the induced spin current as a function of the affinities X_1 , X_2 .

The efficiency of the device can be quantified by the ratio between the power developed by the polarized current J^s and the heat flux J^Q , as defined in Eq. (17). Following the same philosophy as in the usual charge heat engine and refrigerator, we focus on fixed ΔT and analyze the conditions for the maximum possible efficiency within the linear response regime. To this end, we maximize Eq. (17) for fixed ΔT . The maximum value is

$$\eta^{s,\text{he,max}} = \eta_c \frac{\chi^{\text{he}} \sqrt{1 + (ZT)^{s,\text{he}} - 1}}{\sqrt{1 + (ZT)^{s,\text{he}} + 1}}. \quad (37)$$

We have used the following definitions:

$$\chi^{\text{he}} = \frac{\mathcal{L}_{12}^s}{\mathcal{L}_{21}^c}, \quad (ZT)^{s,\text{he}} = \frac{\mathcal{L}_{12}^s \mathcal{L}_{21}^c}{\text{Det} \hat{\mathcal{L}}^{s,\text{he}}}, \quad (38)$$

with $\text{Det} \hat{\mathcal{L}}^{s,\text{he}}$ the determinant of the matrix of Eq. (16). The maximum is found to take place at the value of the voltage bias

$$T \Delta \mu = -\Delta T \frac{\mathcal{L}_{12}^s}{\mathcal{L}_{11}^s R^{\text{he}}} (1 - \sqrt{1 - R^{\text{he}}}), \quad (39)$$

with $R^{\text{he}} = \frac{\mathcal{L}_{12}^s \mathcal{L}_{21}^c}{\mathcal{L}_{11}^s \mathcal{L}_{22}^c}$. The maximum efficiency at fixed ΔT is parametrized by a figure of merit $(ZT)^{s,\text{he}}$, which has the same formal expression as for the charge heat engine. The maximum is achieved for parameters satisfying $(ZT)^{s,\text{he}} \rightarrow \infty$ and it is bounded by $\chi^{\text{he}} \eta_c$. Notice that $\chi^{\text{he}} \leq 1$, and the limit $\chi^{\text{he}} = 1$ corresponds to a fully polarized current. In addition to the definitions of Eqs. (38)–(40), it is important to take into account that for the spin heat engine operational mode to take place, it is necessary to satisfy the following conditions:

$$-\frac{\mathcal{L}_{12}^s}{\mathcal{L}_{11}^c} \Delta T \leq T \Delta \mu \leq 0, \quad \mathcal{L}_{12}^s > 0,$$

$$0 \leq T \Delta \mu \leq -\frac{\mathcal{L}_{12}^s}{\mathcal{L}_{11}^c} \Delta T, \quad \mathcal{L}_{12}^s < 0, \quad (40)$$

From Figs. 5 and 7 we can observe that \mathcal{L}_{21}^c has the same sign of \mathcal{L}_{12}^s and therefore the ratio R^{he} is a positive magnitude

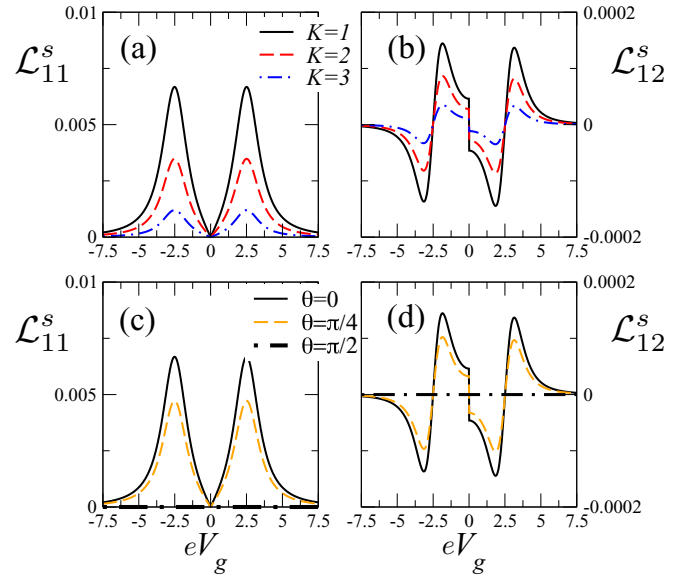


FIG. 7. Onsager coefficients \mathcal{L}_{11}^s and \mathcal{L}_{12}^s corresponding at the spin heat engine at the temperature $k_B T = 0.1\gamma$ and magnetic field $\mu_B B = 5\gamma$, as functions of the gate voltage. Top panels show the K dependence for $\theta = 0$. Lower panels show the θ dependence for $K = 1$. Other details are the same as in Fig. 6.

which is bounded by $0 < R^{\text{he}} < 1$ due to the constraints imposed by $\text{Det} \hat{\mathcal{L}}^{s,\text{he}} > 0$. This determines the selected sign for the root in Eq. (40). In addition, we recall that the coefficients \mathcal{L}_{ij}^s should satisfy the conditions leading to a positive rate of the entropy production given by Eq. (13).

Figure 7 shows the transport coefficients for a finite magnetic field aligned along the direction of the spin-orbit direction in the bar, $\theta = 0$. The overall behavior of these coefficients and their dependence with the interactions K are similar to the charge heat engine (refrigerator) mode. From the definition of the sign ξ in Eq. (16), the coefficient \mathcal{L}_{11}^s has non-negative values and the peaks are at the energies $eV_g = \pm B/2$. The different signs of ξ imply different polarizations of the spin current, hence, different directions of the current along the QSH edge. The coefficient \mathcal{L}_{12}^s does not continuously cross zero as the gate voltage pass from negative to positive values. This is explicitly seen in the discontinuity of \mathcal{L}_{12}^s at $eV_g = 0$, as a consequence of the sign ξ imposed by \mathcal{L}_{11}^s .

In the lower panels of Fig. 7 we show the behavior of these coefficients when the direction of the magnetic field is tilted in an angle θ with respect to the direction of the spin orbit of the QSH. In contrast to the charge regime, the factors $u_{s,\sigma}^2$ enter the coefficients in combinations like $u_{s,\uparrow}^2 - u_{s,\downarrow}^2 = \pm[\cos^2(\theta/2) - \sin^2(\theta/2)]$ leading to a dependence with θ . Explicitly, within the low- T limit, we have for \mathcal{L}_{11}^s ,

$$\mathcal{L}_{11}^s = L_{11}^\uparrow - L_{11}^\downarrow \simeq T \sum_{s,\sigma} (u_{s,\uparrow}^2 - u_{s,\downarrow}^2) \rho_{d,s}(0) I_0(\bar{K})$$

$$= T [\cos^2(\theta/2) - \sin^2(\theta/2)] \sum_s \rho_{d,s}(0) I_0(\bar{K}). \quad (41)$$

A similar expression is found for \mathcal{L}_{12}^s . An interference between the two spin channels is clearly seen as a function of θ .

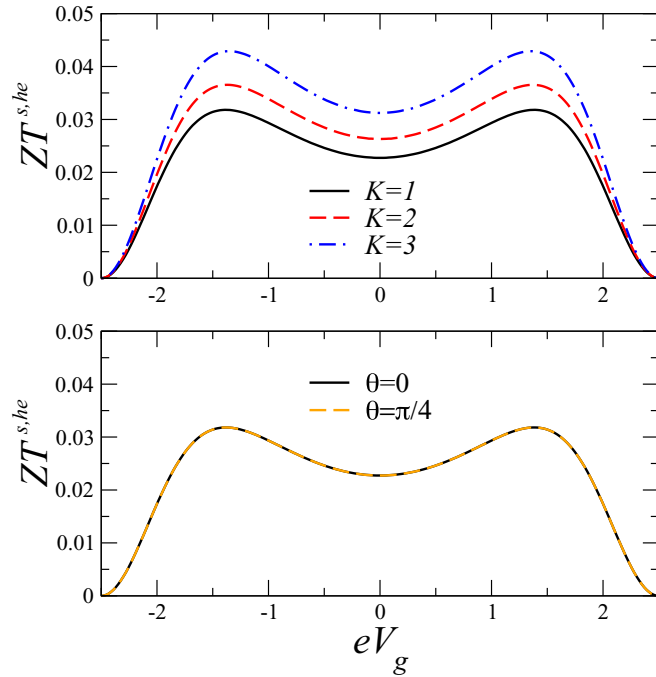


FIG. 8. Figure of merit $ZT^{s,he}$ corresponding at the spin heat engine. Other details are the same as in Fig. 7.

In particular, when the field is perpendicular to the direction of the spin-orbit of the bar, the two coefficients vanish.

The efficiency of the device in this regime is analyzed in Fig. 8, where the figure of merit $(ZT)^{s,he}$ defined in Eq. (39) is shown for the same parameters of Fig. 7. For this mode, the performance is also enhanced for interacting systems with $K \neq 1$. Interestingly, the effect of the alignment of the magnetic field affects identically \mathcal{L}_{11}^s and \mathcal{L}_{12}^s . Hence, the value of ZT is not affected by the tilt angle θ of the magnetic field, as can be seen in the bottom panel of Fig. 8.

C. Spin refrigerator

Finally, we discuss the spin refrigerator mode introduced in Sec. III B 3. As in the heat engine, this regime operates only at finite magnetic field $B \neq 0$.

The coefficient of performance of the device in this case can be quantified by the ratio between the power developed by the polarized heat flux flowing along the helical edge states $J^{Q,s}$ and the charge flux J^C , between the external reservoir and the TI bar, as defined in Eq. (19). Following the same procedure as in the case of the spin heat engine, we fix ΔT and maximize Eq. (19). The maximum value is

$$\eta^{s,fr,max} = \eta_c \frac{\chi^{fri} \sqrt{1 + (ZT)^{s,fri}} - 1}{\sqrt{1 + (ZT)^{s,fri}} + 1}. \quad (42)$$

We have used the following definitions:

$$\chi^{fri} = \frac{\mathcal{L}_{21}^s}{\mathcal{L}_{12}^c}, \quad (ZT)^{s,fri} = \frac{\mathcal{L}_{21}^s \mathcal{L}_{12}^c}{\text{Det} \widehat{\mathcal{L}}^{s,fri}}, \quad (43)$$

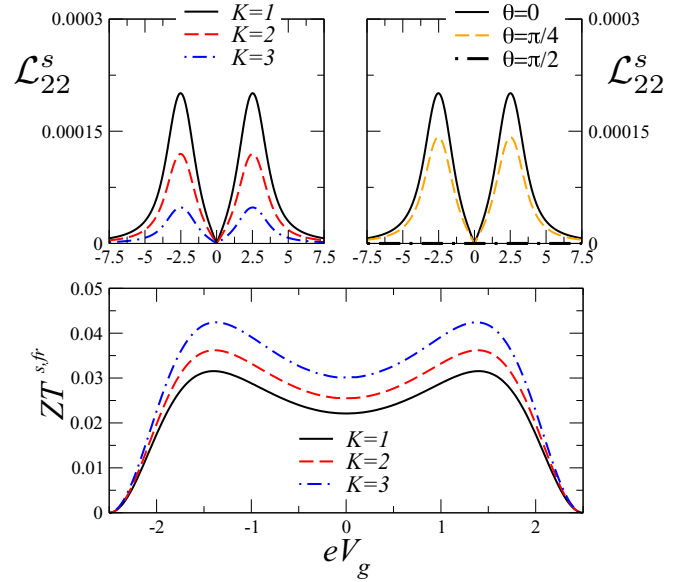


FIG. 9. Onsager coefficients \mathcal{L}_{22}^s (top panels) and figure of merit $ZT^{s,fr}$ (lower panel) corresponding to the spin refrigerator. Other details are the same as in Fig. 7.

with $\text{Det} \widehat{\mathcal{L}}^{s,fri}$ the determinant of the matrix of Eq. (18). The voltage bias corresponding to the maximum is

$$T \Delta \mu = -\Delta T \frac{\mathcal{L}_{22}^s}{\mathcal{L}_{21}^s} (1 - \sqrt{1 - R^{fri}}), \quad (44)$$

where $R^{fri} = \frac{\mathcal{L}_{12}^c \mathcal{L}_{21}^s}{\mathcal{L}_{11}^c \mathcal{L}_{22}^s}$. In this mode the maximum coefficient of performance at fixed ΔT is also parametrized by a figure of merit $(ZT)^{s,fri}$, which has the same formal expression as for the modes previously analyzed. As in the other cases, the maximum is achieved for $(ZT)^{s,fr} \rightarrow \infty$. It is bounded by $\chi^{fr} \eta_c$ and $\chi^{fr} \leq 1$, with the maximum corresponding to a fully polarized current. In addition to the definitions of Eqs. (43)–(45), the following conditions must be satisfied:

$$\begin{aligned} T \Delta \mu < -\frac{\mathcal{L}_{22}^c}{\mathcal{L}_{21}^s} \Delta T, \quad \mathcal{L}_{21}^s > 0, \\ T \Delta \mu > -\frac{\mathcal{L}_{22}^c}{\mathcal{L}_{21}^s} \Delta T, \quad \mathcal{L}_{21}^s < 0. \end{aligned} \quad (45)$$

In this case, the regime is characterized by the coefficients \mathcal{L}_{22}^s , plotted in the top panels of Fig. 9 and \mathcal{L}_{21}^s . As in the spin heat operational mode, this regime implies a proper definition of the sign ξ , such that $\mathcal{L}_{22}^s = \xi (L_{22}^{\uparrow} - L_{22}^{\downarrow}) \geq 0$ to characterize the thermoelectric response. The dependence of the coefficients with the gate voltage and magnetic field is similar to that observed for the spin heat engine. We have verified that the sign ξ , as a function of the gate voltages and magnetic field, is exactly the same within the spin heat and refrigerator regimes. This can be easily verified from the low-temperature expressions of the coefficients in Eq. (29), by noticing that the only difference between L_{11}^s and L_{22}^s is given by the amplitude introduced by the factor $I_n(\bar{K})$ in Eq. (30). As a consequence, the coefficient \mathcal{L}_{21}^s is equal to \mathcal{L}_{12}^s shown in Fig. 7. The coefficient \mathcal{L}_{22}^s and the figure of merit are shown in Fig. 9.

VI. SUMMARY AND DISCUSSION

We have analyzed the thermoelectric response of a pair of helical edge states of a topological insulator coupled to an extra reservoir through a side quantum dot. By applying a gate voltage as well as a magnetic field at the quantum dot, different thermoelectric operational modes can be induced in this device. These include usual charge heat engine and refrigerator, as well as spin heat engine and refrigerator. The latter modes imply the conversion between heat and spin currents and are of interest in spintronics.

In this work we introduced a linear response description, relevant for small bias voltages and temperature differences, and characterize the different regimes by efficiencies or coefficients of performance parametrized by figures of merit. Considering a typical value for the parameter $\gamma \sim 1 \mu eV$ [20], the spin heat engine and spin refrigerator regimes can be achieved with magnetic fields $B \sim 0.1$ T, which are of the order of magnitude of the ones implemented in laboratory to study quantum dots in the Kondo regime [72]. Given the additional fact that our setup is based on a quantum dot coupled albeit not hosted by the topological insulator in the QSH state, the application of a magnetic field is not expected to affect the nature of the helical edge states. For these estimates, the temperatures indicated in Fig. 6 range from $T = 5$ to 40 mK and we see that values of figure of merit as large as $ZT = 5$ can be achieved in the case of noninteracting helical edges. As in the case of the fractional quantum Hall effect studied in Ref. [20], the thermoelectric performance is improved when the many-body interactions are relevant. Hence, for the cases with $K \neq 1$, the above estimates can be improved in a factor depending on \bar{K} , as shown in Eq. (37), and Figs. 4, 7, 8, and 9.

ACKNOWLEDGMENTS

L.A. thanks the Kavli Institute for Theoretical Physics (KITP) for its hospitality during the program Thermodynamics of quantum systems: Measurement, engines and control. E.F. thanks the Department of Physics of the Faculty of Exact and Natural Sciences of the University of Buenos Aires for its hospitality. We acknowledge support from CONICET and MINCyT (PICT 2012-172 and PICT 2014-2049), Argentina, as well as the Alexander von Humboldt Foundation, Germany. This work is supported in part by the National Science Foundation under Grant No. NSF PHY-1748958 at the KITP (L.A.), and under Grant No. DMR-1725401 at the University of Illinois (E.F.).

APPENDIX: DENSITY OF STATES OF THE HELICAL EDGES

The derivation of the density of states of the chiral Luttinger liquid $\rho_\sigma(\omega)$ entering in Eq. (22) follows from the Hamiltonian in Eq. (2) and can be obtained by using standard

bosonization technique as presented in Ref. [21]. Here we summarize the main steps.

Starting from the definition of the greater Green function $ig_\downarrow^\gt(t-t')$ and the expression of the fermionic fields in terms of the bosonic ones in Eq. (4) one arrives at

$$\begin{aligned} ig_\downarrow^\gt(t-t') &= \langle \psi_\downarrow(t) \psi_\downarrow^\dagger(t') \rangle \\ &= \frac{1}{2\pi a} \langle e^{iK_+\phi_\downarrow(t)} e^{iK_-\phi_\uparrow(t)} e^{-iK_+\phi_\downarrow(t')} e^{-iK_-\phi_\uparrow(t')} \rangle \\ &= \frac{1}{2\pi a} e^{K_+^2 D_\downarrow^\gt(t-t')} e^{K_-^2 D_\uparrow^\gt(t-t')}, \end{aligned} \quad (\text{A1})$$

where $D_\sigma^\gt(t-t') = D_\sigma^\lt(t'-t) = \langle \phi_\sigma(t) \phi_\sigma(t') \rangle - \frac{1}{2} \langle \phi_\sigma^2(t) \rangle - \frac{1}{2} \langle \phi_\sigma^2(t') \rangle$, for $t > t'$ is the bosonic propagator associated at the σ channel in Eq. (2). The latter is given by the following expression:

$$D_\sigma^\gt(t-t') = K \text{Ln} \left[\frac{\sinh(i\pi T)}{\sinh[\pi T(t'-t+ia)]} \right]. \quad (\text{A2})$$

Inserting Eq. (A2) into Eq. (A1) the greater Green function can be simple written as

$$\begin{aligned} g_\downarrow^\gt(t-t') &= \frac{-i}{2\pi a} \left[\frac{\sinh(i\pi T)}{\sinh[\pi T(t'-t+ia)]} \right]^{(K_+^2+K_-^2)K}, \\ g_\downarrow^\gt(t-t') &= \frac{-i}{2\pi a} \left[\frac{\sinh(i\pi T)}{\sinh[\pi T(t'-t+ia)]} \right]^{\bar{K}}, \end{aligned} \quad (\text{A3})$$

where $\bar{K} \equiv (K_+^2 + K_-^2)K = \frac{1}{2}(\frac{1}{K} + K)$.

The lesser Green function is obtained through the relation $g_\sigma^\lt(t-t') = -g_\sigma^\gt(t'-t)$,

$$g_\downarrow^\lt(t-t') = \frac{i}{2\pi a} \left[\frac{\sinh(i\pi T)}{\sinh[\pi T(t-t'+ia)]} \right]^{\bar{K}}, \quad (\text{A4})$$

Note that the left and right movers share the same temperature and, as a consequence, there is no spin dependence in the explicit expressions of the above Green functions.

Transforming Fourier to the frequency domain we have

$$g_\sigma^\lt(\omega) = ia^{\bar{K}-1} \frac{(2\pi T)^{\bar{K}-1}}{2\pi \Gamma(\bar{K})} e^{-\omega/2T} |\Gamma(\bar{K}/2 + i\omega/2\pi T)|^2. \quad (\text{A5})$$

Finally, the density of states $\rho_\sigma(\omega)$ can be introduced through the identity $g_\sigma^\lt(\omega) = 2\pi i \rho_\sigma(\omega) f(\omega)$, where $f(\omega)$ is the Fermi distribution and $\Gamma(z)$ is the Gamma function. The final expression for the densities of states, Eq. (22) reads

$$\rho_\sigma(\omega) = a^{\bar{K}-1} \frac{(2\pi T)^{\bar{K}-1}}{\Gamma(\bar{K})} \left| \frac{\Gamma(\bar{K}/2 + i\omega/2\pi T)}{\Gamma(1/2 + i\omega/2\pi T)} \right|^2. \quad (\text{A6})$$

[1] X. G. Wen, Topological orders and Edge excitations in FQH states, *Adv. Phys.* **44**, 405 (1995).

[2] B. I. Halperin, Quantized Hall conductance, current-carrying edge states, and the existence of extended states in a two-dimensional disordered potential, *Phys. Rev. B* **25**, 2185 (1982).

[3] R. B. Laughlin, Quantized Hall conductivity in two dimensions, *Phys. Rev. B* **23**, 5632 (1981).

[4] M. Büttiker, Absence of backscattering in the quantum Hall effect in multiprobe conductors, *Phys. Rev. B* **38**, 9375 (1988).

[5] E. Fradkin, *Field Theories of Condensed Matter Systems*, 2nd ed. (Cambridge University Press, Cambridge, UK, 2013).

- [6] C. L. Kane and E. J. Mele, Z_2 Topological Order and the Quantum Spin Hall Effect, *Phys. Rev. Lett.* **95**, 146802 (2005).
- [7] C. L. Kane and E. J. Mele, Quantum Spin Hall Effect in Graphene, *Phys. Rev. Lett.* **95**, 226801 (2005).
- [8] B. A. Bernevig, T. L. Hughes, and S.-C. Zhang, Quantum spin Hall effect and topological phase transition in HgTe quantum wells, *Science* **314**, 1757 (2006).
- [9] C. Wu, B. A. Bernevig, and S.-C. Zhang, Helical Liquid and the Edge of Quantum Spin Hall Systems, *Phys. Rev. Lett.* **96**, 106401 (2006).
- [10] C. Xu and J. Moore, Stability of the quantum spin Hall effect: Effects of interactions, disorder, and Z_2 topology, *Phys. Rev. B* **73**, 045322 (2006).
- [11] M. König, S. Wiedmann, C. Brüne, A. Roth, H. Buhmann, L. W. Molenkamp, X. L. Qi, and S.-C. Zhang, Quantum spin Hall insulator state in HgTe quantum wells, *Science* **318**, 766 (2007).
- [12] C. L. Kane and M. P. A. Fisher, Thermal Transport in a Luttinger Liquid, *Phys. Rev. Lett.* **76**, 3192 (1996).
- [13] C. L. Kane and M. P. A. Fisher, Quantized thermal transport in the fractional quantum Hall effect, *Phys. Rev. B* **55**, 15832 (1997).
- [14] C. de C. Chamon and E. Fradkin, How to observe distinct universal conductances in tunneling to quantum Hall states: having the right contacts, *Phys. Rev. B* **56**, 1212 (1997).
- [15] E.-A. Kim and E. Fradkin, Interedge tunneling in quantum Hall line junctions, *Phys. Rev. B* **67**, 045317 (2003).
- [16] A. M. Chang, Chiral Luttinger liquids at the fractional quantum Hall edge, *Rev. Mod. Phys.* **75**, 1449 (2003).
- [17] C. Glattli, Tunneling experiments in the fractional quantum Hall effect regime, *Séminaire Poincaré* **2**, 75 (2004).
- [18] S. Takei, M. Milletari, and B. Rosenow, Nonequilibrium electron spectroscopy of Luttinger liquids, *Phys. Rev. B* **82**, 041306(R) (2010).
- [19] T. Karzig, G. Refael, L. I. Glazman, and F. von Oppen, Energy Partitioning of Tunneling Currents into Luttinger Liquids, *Phys. Rev. Lett.* **107**, 176403 (2011).
- [20] P. Roura-Bas, L. Arrachea, and E. Fradkin, Enhanced thermoelectric response in the fractional quantum Hall effect, *Phys. Rev. B* **97**, 081104 (2018).
- [21] T. Giamarchi, *Quantum Physics in One Dimension* (Oxford University Press, Oxford, 2004).
- [22] G. Granger, J. P. Eisenstein, and J. L. Reno, Observation of Chiral Heat Transport in the Quantum Hall Regime, *Phys. Rev. Lett.* **102**, 086803 (2009).
- [23] L. Arrachea and E. Fradkin, Chiral heat transport in driven quantum Hall and quantum spin Hall edge states, *Phys. Rev. B* **84**, 235436 (2011).
- [24] S. G. Nam, E. H. Hwang, and H. J. Lee, Thermoelectric Detection of Chiral Heat Transport in Graphene in the Quantum Hall Regime, *Phys. Rev. Lett.* **110**, 226801 (2013).
- [25] S. Jezouin, F. D. Parmentier, A. Anthore, U. Gennser, A. J. Cavanna, and F. Pierre, Quantum limit of heat flow across a single electronic channel, *Science* **342**, 601 (2013).
- [26] A. Cappelli, M. Huerta, and G. Zemba, Thermal transport in chiral conformal theories and hierarchical quantum Hall states, *Nucl. Phys. B* **636**, 568 (2002).
- [27] E. Grosfeld and S. Das, Probing the Neutral Edge Modes in Transport across a Point Contact via Thermal Effects in the Read-Rezayi Non-Abelian Quantum Hall States, *Phys. Rev. Lett.* **102**, 106403 (2009).
- [28] H. Aita, L. Arrachea, C. Naón, and E. Fradkin, Heat transport through quantum Hall edge states: Tunneling versus capacitive coupling to reservoirs, *Phys. Rev. B* **88**, 085122 (2013).
- [29] G. Viola, S. Das, E. Grosfeld, and A. Stern, Thermoelectric Probe for Neutral Edge Modes in the Fractional Quantum Hall Regime, *Phys. Rev. Lett.* **109**, 146801 (2012).
- [30] I. Gurman, R. Sabo, M. Heiblum, V. Umansky, and D. Mahalu, Extracting net current from an upstream neutral mode in the fractional quantum Hall regime, *Nat. Commun.* **3**, 1289 (2012).
- [31] C. Altimiras, H. le Sueur, U. Gennser, A. Cavanna, D. Mailly, and F. Pierre, Tuning Energy Relaxation Along Quantum Hall Channels, *Phys. Rev. Lett.* **105**, 226804 (2010).
- [32] V. Venkatchalam, S. Hart, L. Pfeiffer, K. West, and A. Yacoby, Local thermometry of neutral modes on the quantum Hall edge, *Nat. Phys.* **8**, 676 (2012).
- [33] C. Altimiras, H. le Sueur, U. Gennser, A. Anthore, A. Cavanna, D. Mailly, and F. Pierre, Chargeless Heat Transport in the Fractional Quantum Hall Regime, *Phys. Rev. Lett.* **109**, 026803 (2012).
- [34] M. Banerjee, M. Heiblum, A. Rosenblatt, Y. Oreg, D. E. Feldman, A. Stern, and V. Umansky, Observed quantization of anyonic heat flow, *Nature (London)* **545**, 75 (2017).
- [35] A. Aharon, Y. Oreg, and A. Stern, Phenomenological theory of heat transport in the fractional quantum Hall effect, [arXiv:1805.09229](https://arxiv.org/abs/1805.09229).
- [36] R. Sánchez, B. Sothmann, and A. N. Jordan, Chiral Thermoelectrics with Quantum Hall Edge States, *Phys. Rev. Lett.* **114**, 146801 (2015).
- [37] P. Samuelsson, S. Kheradsoud, and B. Sothmann, Optimal Quantum Interference Thermoelectric Heat Engine with Edge States, *Phys. Rev. Lett.* **118**, 256801 (2017).
- [38] L. Vannucci, F. Ronetti, G. Dolcetto, M. Carrega, and M. Sassetti, Interference-induced thermoelectric switching and heat rectification in quantum Hall junctions, *Phys. Rev. B* **92**, 075446 (2015).
- [39] X.-Q. Yu, Z.-G. Zhu, G. Su, and A. P. Jauho, A spin caloritronic battery, *Phys. Rev. Appl.* **8**, 054038 (2017).
- [40] F. Ronetti, L. Vannucci, G. Dolcetto, M. Carrega, and M. Sassetti, Spin-thermoelectric transport induced by interactions and spin-flip processes in two dimensional topological insulators, *Phys. Rev. B* **93**, 165414 (2016).
- [41] S.-Y. Hwang, R. Lopez, M. Lee, and D. Sanchez, Nonlinear spin-thermoelectric transport in two-dimensional topological insulators, *Phys. Rev. B* **90**, 115301 (2014).
- [42] P.-H. Chang, M. S. Bahrmy, N. Nagaosa, and B. K. Nikolic, Giant thermoelectric effect in graphene-based topological insulators with nanopores, *Nano Lett.* **14**, 3779 (2014).
- [43] D. G. Rothe, E. M. Hankiewicz, B. Trauzettel, and M. Guigou, Spin-dependent thermoelectric transport in HgTe/CdTe quantum wells, *Phys. Rev. B* **86**, 165434 (2012).
- [44] B. Sothmann and E. M. Hankiewicz, Fingerprint of topological Andreev bound states in phase-dependent heat transport, *Phys. Rev. B* **94**, 081407(R) (2016).
- [45] A. Mani and C. Benjamin, Helical thermoelectrics and refrigeration, *Phys. Rev. E* **97**, 022114 (2018).
- [46] M. Josefsson, A. Svilans, A. M. Burke, E. A. Hoffmann, S. Fahlvik, C. Thelander, M. Leijnse, and H. Linke, A

- quantum-dot heat engine operating close to the thermodynamic efficiency limits, *Nat. Nanotechnol.* **13**, 920 (2018).
- [47] G. Benenti, G. Casati, K. Saito, and R. S. Whitney, Fundamental aspects of steady-state conversion of heat to work at the nanoscale, *Phys. Rep.* **694**, 1 (2017).
- [48] O. Entin-Wohlman, Y. Imry, and A. Aharony, Enhanced performance of joint cooling and energy production, *Phys. Rev. B* **91**, 054302 (2015).
- [49] H. Thierschmann, R. Sánchez, B. Sothmann, F. Arnold, C. Heyn, W. Hansen, H. Buhmann, and L. W. Molenkamp, Three-terminal energy harvester with coupled quantum dots, *Nat. Nanotechnol.* **10**, 854 (2015).
- [50] G. Tang, J. Thingna, and J. Wang, Thermodynamics of energy, charge, and spin currents in a thermoelectric quantum-dot spin valve, *Phys. Rev. B* **97**, 155430 (2018).
- [51] F. Dolcini, Full electrical control of charge and spin conductance through interferometry of edge states in topological insulators, *Phys. Rev. B* **83**, 165304 (2011).
- [52] F. Romeo, R. Citro, D. Ferraro, and M. Sassetti, Electrical switching and interferometry of massive Dirac particles in topological insulator constrictions, *Phys. Rev. B* **86**, 165418 (2012).
- [53] B. Rizzo, L. Arrachea, and M. Moskalets, Transport phenomena in helical edge states interferometers: A Green's function approach, *Phys. Rev. B* **88**, 155433 (2013).
- [54] F. Crépin, J. C. Budich, F. Dolcini, P. Recher, and B. Trauzettel, Renormalization group approach for the scattering off a single Rashba impurity in a helical liquid, *Phys. Rev. B* **86**, 121106(R) (2012).
- [55] G. Dolcetto, F. Cavaliere, D. Ferraro, and M. Sassetti, Generating and controlling spin-polarized currents induced by a quantum spin Hall antidot, *Phys. Rev. B* **87**, 085425 (2013).
- [56] J. Väyrynen, M. Goldstein, and L. I. Glazman, Helical Edge Resistance Introduced by Charge Puddles, *Phys. Rev. Lett.* **110**, 216402 (2013).
- [57] J. Väyrynen, M. Goldstein, Y. Gefen, and L. I. Glazman, Resistance of helical edges formed in a semiconductor heterostructure, *Phys. Rev. B* **90**, 115309 (2014).
- [58] A. M. Lunde and G. Platero, Helical edge states coupled to a spin bath: Current-induced magnetization, *Phys. Rev. B* **86**, 035112 (2012).
- [59] K. T. Law, C. Y. Seng, P. A. Lee, and T. K. Ng, Quantum dot in a two-dimensional topological insulator: The two-channel Kondo fixed point, *Phys. Rev. B* **81**, 041305 (2010).
- [60] T. L. Schmidt, S. Rachel, F. von Oppen, and L. I. Glazman, Inelastic Electron Backscattering in a Generic Helical Edge Channel, *Phys. Rev. Lett.* **108**, 156402 (2012).
- [61] V. Cheianov and L. I. Glazman, Mesoscopic Fluctuations of Conductance of a Helical Edge Contaminated by Magnetic Impurities, *Phys. Rev. Lett.* **110**, 206803 (2013).
- [62] T. Posske, C.-X. Liu, J. C. Budich, and B. Trauzettel, Exact Results for the Kondo Screening Cloud of Two Helical Liquids, *Phys. Rev. Lett.* **110**, 016602 (2013).
- [63] T. Posske and B. Trauzettel, Direct proportionality between the Kondo cloud and current cross correlations in helical liquids, *Phys. Rev. B* **89**, 075108 (2014).
- [64] B. Probst, P. Virtanen, and P. Recher, Controlling spin polarization of a quantum dot via a helical edge state, *Phys. Rev. B* **92**, 045430 (2015).
- [65] A. Rod, G. Dolcetto, S. Rachel, and T. L. Schmidt, Transport through a quantum spin Hall antidot as a spectroscopic probe of spin textures, *Phys. Rev. B* **94**, 035428 (2016).
- [66] G. Tang, F. Xu, S. Mi, and J. Wang, Spin-resolved electron waiting times in a quantum-dot spin valve, *Phys. Rev. B* **97**, 165407 (2018).
- [67] B. Rizzo, A. Camjayi, and L. Arrachea, Transport in quantum spin Hall edges in contact to a quantum dot, *Phys. Rev. B* **94**, 125425 (2016).
- [68] Q. Meng, S. Vishveshwara, and T. L. Hughes, Spin-transfer torque and electric current in helical edge states in quantum spin Hall devices, *Phys. Rev. B* **90**, 205403 (2014).
- [69] L. Arrachea and F. von Oppen, Nanomagnet coupled to quantum spin Hall edge: An adiabatic quantum motor, *Physica E* **74**, 596 (2015).
- [70] P. G. Silvestrov, P. Recher, and P. W. Brouwer, Noiseless manipulation of helical edge state transport by a quantum magnet, *Phys. Rev. B* **93**, 205130 (2016).
- [71] C. L. Kane and M. P. A. Fisher, Transmission through barriers and resonant tunneling in an interacting one-dimensional electron gas, *Phys. Rev. B* **46**, 15233 (1992).
- [72] S. M. Cronenwett, T. H. Oosterkamp, and L. P. Kouwenhoven, A tunable Kondo effect in quantum dots, *Science* **281**, 540 (1998).